Compression Testing and FEA of 8-in. (200-mm) Diameter AWWA C900 DR14 iPVC Pipe

Shih-Hung Chiu

Gersena Banushi

Shakhzod Takhirov

Kenichi Soga

CSI Report 2026/03
Center for Smart Infrastructure (CSI)
Department of Civil and Environmental Engineering
University of California, Berkeley August 2026

EXECUTIVE SUMMARY

This report presents the results of the experimental compression testing of an 8-inch AWWA C900 DR14 iPVC pipe under axial force. The pipe is resistant to corrosion and can tolerate significant deformations to enhance seismic resilience. The compression test was conducted under a monotonic force applied at the center of the specimens perpendicular to the pipeline direction. It was tested up to severe pipe damage or significant water leakage. Notable local buckling on the west pipe induced rotational movements, leading to significant compressive forces and eventual failure at the sleeve-west pipe interface. Distributed fiber optic sensors were used to provide more insight into deformation and failure mechanisms. Axial strain measurements showed compressive strains across all locations, with the strain profiles indicating a stiffer fitting due to its thicker wall. Hoop strain results revealed tensile strains caused by Poisson's effect, with eccentric expansion reflecting the local buckling influence.

Keywords: ***iPVC pipe, water pipelines, fiber optic, leakage, sensors.***

ACKNOWLEDGMENTS

The funding for this project was provided by the East Bay Municipal Utility District (EBMUD) and PPI Pipe. The completion of the work would not be possible without the support of John Kochan, Irik Larson, and Phillip Wong of the University of California, Berkeley. Active involvement and guidance from David Katzev of EBMUD and Marcus Min of PPI America, Inc. are greatly appreciated.

DISCLAIMER

Any opinions, findings, conclusions, or recommendations expressed in this material are those of the author(s) and do not necessarily reflect those of the University of California, Berkeley.

CONTENTS

LIST OF FIGURES

LIST OF TABLES

1 Introduction

This report summarizes the experimental results of a compression test performed on 8-inch AWWA C900 DR14 iPVC pipes. The iPVC pipes are known for their corrosion resistance and ability to tolerate large deformations, enhancing seismic resilience in pipeline systems. The experiment involved joining two identical pipes using a fitting with a circular rubber gasket featuring multiple teeth, specifically the ReiberLok gasket. This gasket serves to prevent water leakage, while the teeth act as a locking mechanism, restraining the pipes from separating. Figure 1-1 and Figure 1-2 illustrate the fully assembled fitting and the cross-section of the fitting, and the ReiberLok gasket, respectively.

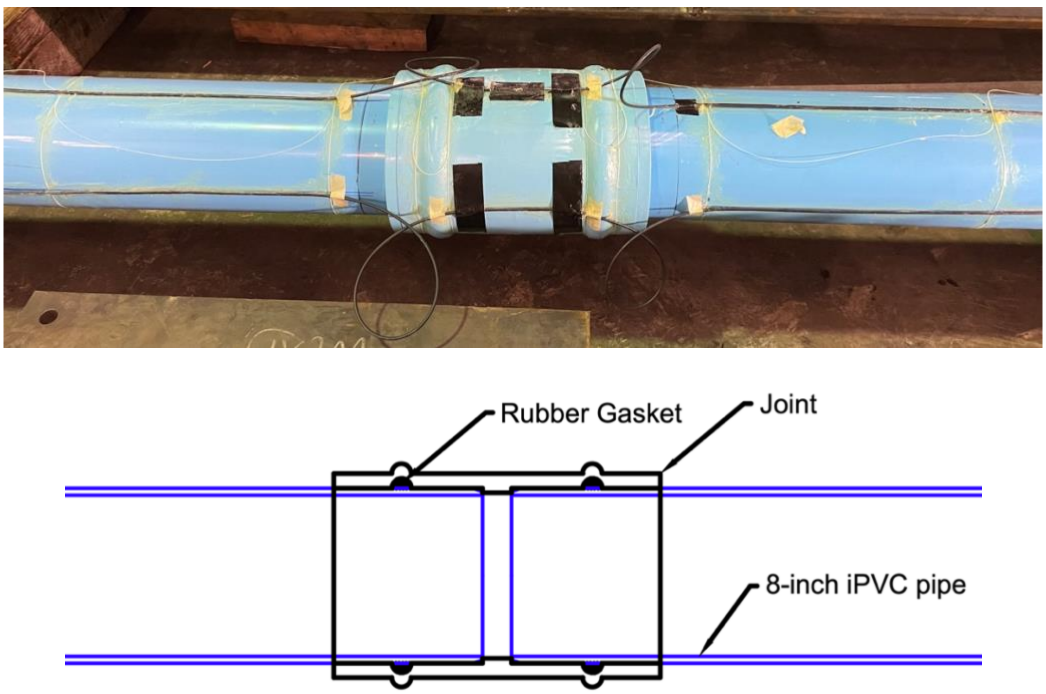

Figure 1-1 Schematic of the fitting of AWWA C900 DR14 iPVC pipe

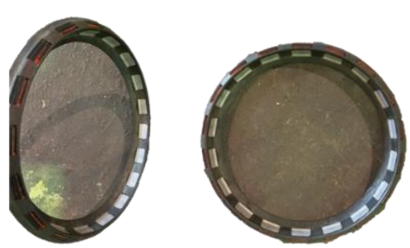

(a) ReiberLok gasket

Figure 1-2 Gaskets for the specimens

Distributed fiber optic sensors (DFOS) were employed to measure continuous strain development along the longitudinal and circumferential directions. Position transducers tracked specimen movement, load cells measured applied force, and pressure gauges monitored internal water pressure. Based on experimental data, the follow sections provide detailed information about the modes and mechanisms of failure.

2 Experimental Setup

A special experimental setup was designed and constructed to conduct tension and compression tests. Small modifications were introduced into the setup to accommodate changes in the force direction in the tension or compression test. This section describes the setup for the tension test.

Experimental setup. The testing apparatus was designed as a self-reacting system and represents a closed-loop frame. It comprised two 16.5-ft long W14x132 wide flange structural beams and two 7-ft long W10x112 wide flange structural beams. Three holes reinforced with stiffeners were introduced into the short beams. Two outer holes of the short beams were used for assembling the closed-loop frame and bolting all beams together, as presented in the schematic drawing shown in Figure 2-1. The center hole in the short beam (the red beam in Figure 2-1) was used as an attachment point for the loading side of the pipe. The loading rod was then inserted into the hole as shown in Figure 2-1.

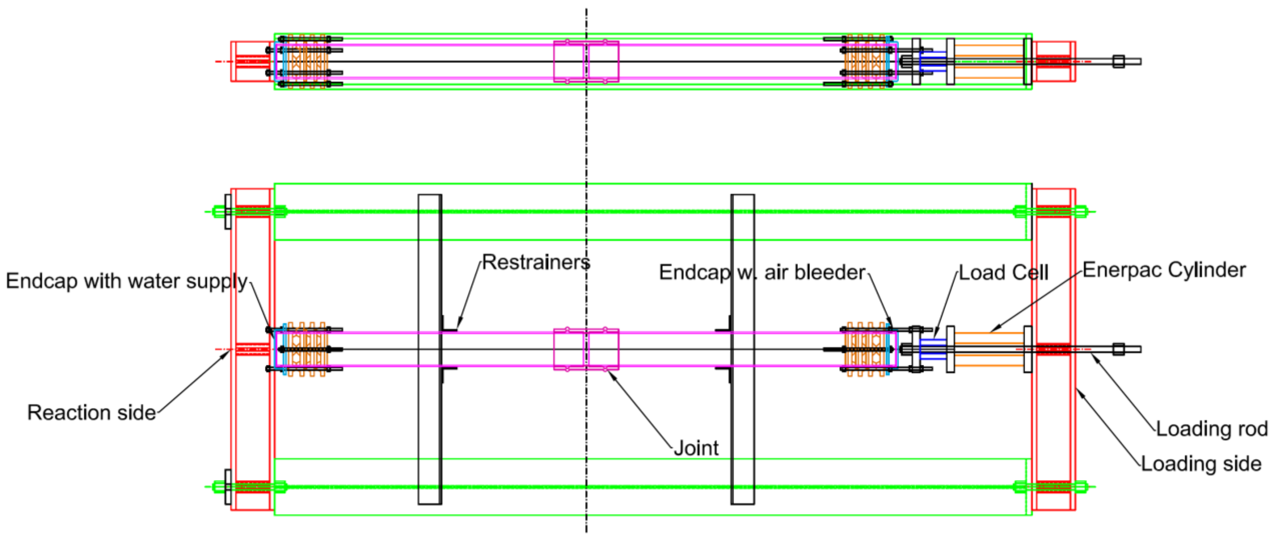

Figure 2-1 Drawing of the experimental setup

To minimize the global buckling of the test specimen, two restrainer frames were introduced as shown in Figure 2-1. The load was applied by a hydraulic cylinder with an ultimate load capacity of 132-kips. The stroke capacity of the cylinder was greater than 6-in. A hollow hydraulic cylinder was selected for this setup to ensure that the loading rod could be fed through the hole in the W10x112 beam and locked with a nut and a washer plate. The latter locking nut was placed far enough from the W10x112 beam to accommodate displacement toward the joint. As shown in Figure 2-2, a load cell was installed between the hydraulic cylinder and the short beam.

Figure 2-2 Hydraulic cylinder and load cell on the loading side

To enable force transfer to the pipe on both the reaction and the loading sides, a set of three MegaLug 2008PV restrainers were installed and connected to the endcap on each side. The rest of the details differed slightly for the reaction and loading sides. On the reaction side, all MegaLug restrainers were engaged together by utilizing four D3/4-in high-strength threaded rods attached to the short I-beam, as shown in Figure 2-3. The endcap was in full contact with the W10x112 beam to make sure that all the forces would be transferred to the beam and not to the rod.

Figure 2-3 Attachment details on the reaction side

Two iPVC pipes were cut to the same length to ensure that the sleeve joint was in the middle of the specimen. As noted earlier, special restrainer frames were introduced to minimize the global buckling of the test specimen. They were installed on both sides of the joint as shown in Figure 2-4.

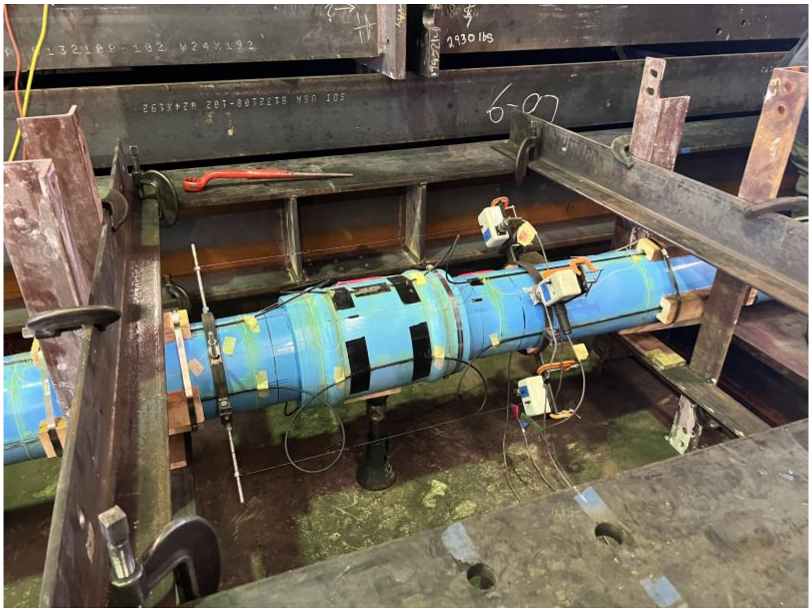

Figure 2-4 Attachment details on the loading side

Figure 2-5 is a photo of the final setup, showing a view from the loading side. Figure 2-6 is a photo of the experimental setup with the specimen during a test, showing a side view.

Figure 2-5 Photo of the completely assembled test setup: view from the reaction side

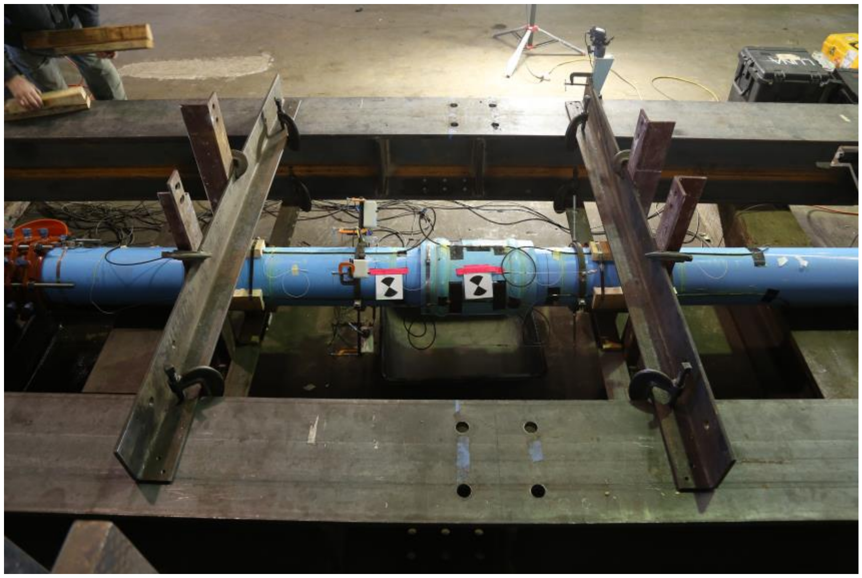

Figure 2-6 Photo of the experimental setup and the test specimen during the test: a side view

Test specimen. One test specimen was tested in compression. The test was conducted on 03/18/2024, and both iPVC pipes were fully inserted into the sleeve joint. Reiberlok gaskets (PN 012-MWG-1023) was installed in the sleeve joint prior to the insertion of the iPVC pipes, as shown in Figure 2-7.

Figure 2-7 Reiberlok gaskets were installed into the sleeve joint

As instructed by PPI, only the beveled sides of the iPVC pipe, shown in Figure 2-8, were driven into the sleeve joint.

Figure 2-8 The beveled sides of the supplied iPVC pipes were inserted into the sleeve joint

Prior to the test, the specimen was filled with water and pressurized to about 65 psi. A monotonically increased load was applied. Table 2-1 provides a summary of the testing steps.

Table 2-1 Summary of test runs and recorded data files

No	Specimen name	Date	Data files	Note
1	CSI-2023-PPI-C01	03/18/2024	Run002	Water pressurization
2	CSI-2023-PPI-C01	03/18/2024	Run003	Compression test

3 Instrumentation

The instrumentation consisted of conventional sensors (position transducer, load cell, pressure gage) and distributed fiber optic sensors. The instrumentation plan is discussed in the following sections.

3.1 Conventional Instruments

The experimental setup and the specimen were extensively instrumented. The instrumentation consisted of a load cell, position transducers measuring the displacement of the pipes across the joint, and a position transducer monitoring the displacement of the sleeve on the loading side, as summarized in Table 3-1. In addition, fiber optic sensor was utilized, which will be discussed in detail in the respective section.

Table 3-1 Summary of conventional instrumentation

Column No in data file	Channel name	Description	Measurement, units
3	Pacific - 8 (0:0:7) loadcell	Load cell	Applied force, lbs
4	Pacific - 73 (0:9:0) wp5	Position transducer	Displacement of sleeve (loading side), in
5	Pacific - 74 (0:9:1) waterpress	Pressure gage	Water pressure, psi
6	Pacific - 75 (0:9:2) novo1	Position transducer	Displacement of MegaLug (reaction side), in
7	Pacific - 76 (0:9:3) novo2	Position transducer	Displacement of MegaLug (loading side), in
8	Pacific - 77 (0:9:4) wp1	Position transducer	Displacement across the joint, in
9	Pacific - 78 (0:9:5) wp2	Position transducer	Displacement across the joint, in
10	Pacific - 79 (0:9:6) wp3	Position transducer	Displacement across the joint, in
11	Pacific - 80 (0:9:7) wp4	Position transducer	Displacement across the joint, in

Figure 3-1 shows position transducers used for measuring displacement across the joint and displacement of the sleeve with respect to the pipe on the loading side. A schematic drawing of the instrumentation locations is given in Figure 3-2.

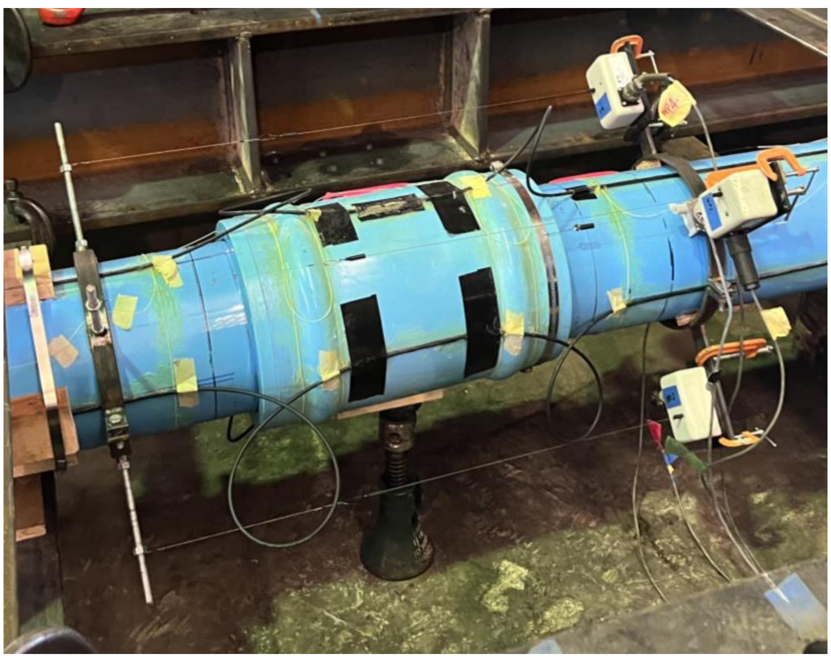

Figure 3-1 Position transducers for joint displacement monitoring

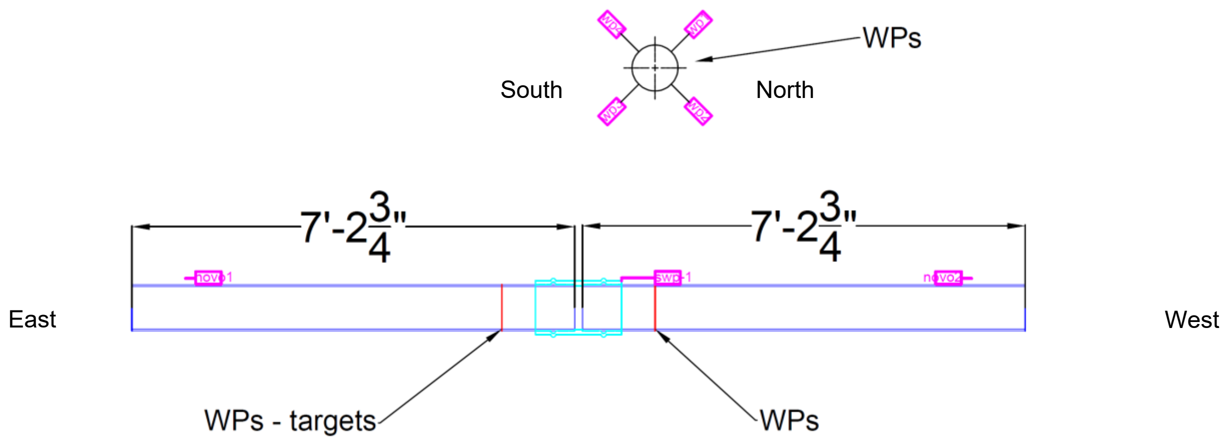

Figure 3-2 Conventional instrumentation plan

A typical installation of the position transducer monitoring MegaLug's displacement (the pipe on the loading side is shown) is shown in Figure 3-3.

Figure 3-3 Transducer for monitoring the displacement of MegaLug

3.2 Fiber Optic Sensors

Two types of fiber optic cables manufactured by NanZee Sensing Technology Co. were used; (a) 5 mm diameter armored cable (NanZee 5mm) and (b) 0.9 mm diameter cable (NanZee 0.9mm). Huntsman Araldite 2021-1 epoxy was used to attach the fiber optic cables to the pipes. Figure 3-4 shows the layout and locations of the sensors. NanZee 5mm cables (blue lines) were used in the longitudinal direction to mimic the use on construction sites. They were attached on both pipes, 90 degrees apart, numbered F9-F16. On the other hand, to better understand the deformation mechanism of the pipes, a thiner NanZee 0.9mm (red lines) cable was used for measuring circumferential strains, numbered F1-F8. Two circumferential sensors with about 18-inch spacing were installed on both pipes. In addition, two circumferential sensors were placed on both sides of each of the gaskets. Since there are two gaskets in the fitting to lock the two pipes, there are in total four circumferential sensors on the fitting. The local names of DFOS are listed in Table 3-2.

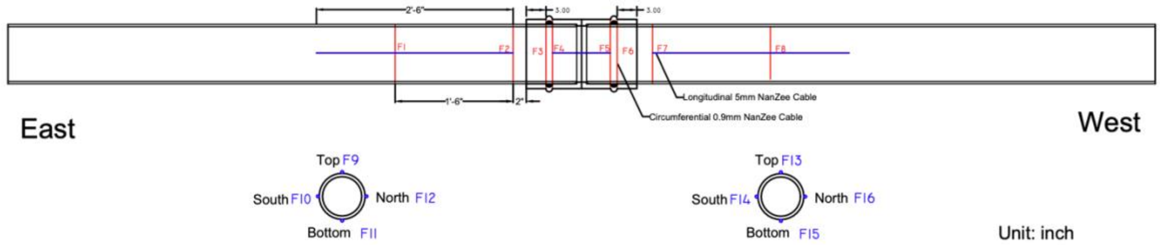

Figure 3-4 Instrumentation plan of fiber optic sensors of the specimens

Table 3-2 Summary of fiber optic sensors

Instrument	Location	Local Instrument Name
DFOS	28.375 inch west of center, Circumferential	F1
	10.375 inch west of center, Circumferential	F2
	5.375 inch west of center, Circumferential	F3
	4.375 inch west of center, Circumferential	F4
	4.375 inch east of center, Circumferential	F5
	5.375 inch east of center, Circumferential	F6
	10.375 inch east of center, Circumferential	F7
	28.375 inch east of center, Circumferential	F8
	West pipe, Top, Longitudinal	F9
	West pipe, South, Longitudinal	F10
	West pipe, Bottom, Longitudinal	F11
	West pipe, North, Longitudinal	F12
	East pipe, Top, Longitudinal	F13
	East pipe, South, Longitudinal	F14
	East pipe, Bottom, Longitudinal	F15
	East pipe, North, Longitudinal	F16

A Rayleigh-based optical frequency domain reflectometry (OFDR), Luna ODiSI 6100 series, was used in the experiments for data acquisition. The analyzer is capable of measuring up to 100 meters long fiber optic cable with an accuracy of less than ±1 micro strain when taking a measurement every 0.65mm. Appendix A provides more information about the cables and the analyzer.

4 Test Results

All test results are discussed in this section. In addition, a summary of the failure mode and performance of the 8 inches AWWA C900 DR14 iPVC pipe is included.

4.1 Axial Force and Joint Opening

The pipes were filled with water and pressurized to about 65 psi. A monotonic force pusing inward of the fitting was applied on the longitudinal axis of the pipeline. The load-displacement curve is shown in Figure 4-1. The displacement across the joint was calculated by averaging the readings of four position transducers placed across the joint, notated as "average joint closing". The specimen reached its peak compressive resistance at 98.8 kips of force at displacement across the joint of about 3.46 inch.

The load-displacement curve during the test exhibited a multi-step pattern, with notable steps occurring at 20 kips, 62 kips, and 98.8 kips, followed by a decrease to 60 kips. The first step, around 20 kips, may be attributed to the readjustment of the rubber gasket's position. The second step is due to local buckling on the west pipe. At the peak load of 98.8 kips, significant local buckling was observed on the west pipe, causing considerable rotation of the joint. This introduced large moments and rotation around the fitting, resulting in substantial deformations of the pipe. As a result of the deformation, the force did not increase further, but the deformation continued to grow. Notably, water leakage was not detected until the specimen was unloaded from a joint compression of 4.9 inches. The joint's deformation mechanism is complex and will be further discussed in the following section using results from Distributed Fiber Optic Sensing (DFOS).

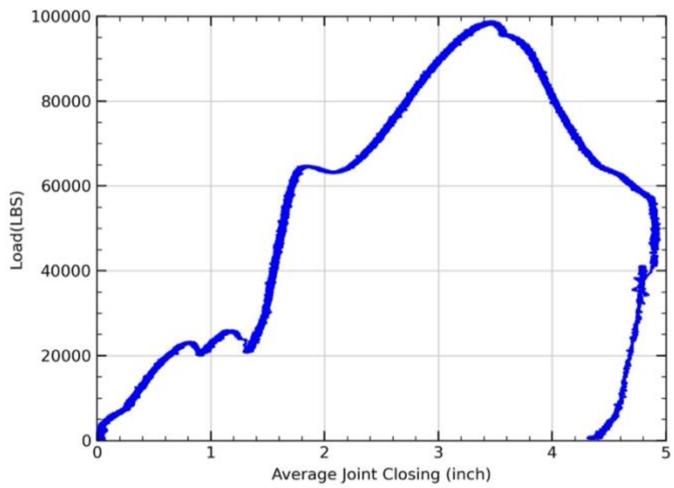

Figure 4-1 Force versus average joint closing for the sleeve with Reiberlok gasket

4.2 Deformation and Failure Modes

Figure 4-2 shows that large deformation occurred at the interface of the sleeve and the west pipe, with evident local buckling. Particularly, local buckling was noted on the west pipe near the edge of the fitting, as shown in Figure 4-2 (a). This local buckling induced a rotation, and as the compressive force intensified, the fitting's rotation imposed significant compressive force on the west pipe.

As described earlier, no water leakage occurred during compression loading. The pipe failed after unloading and water leakage then started. Figure 4-2 (b) and (c) show the failure occurring adjacent to the fitting, coinciding with the area of high compression.

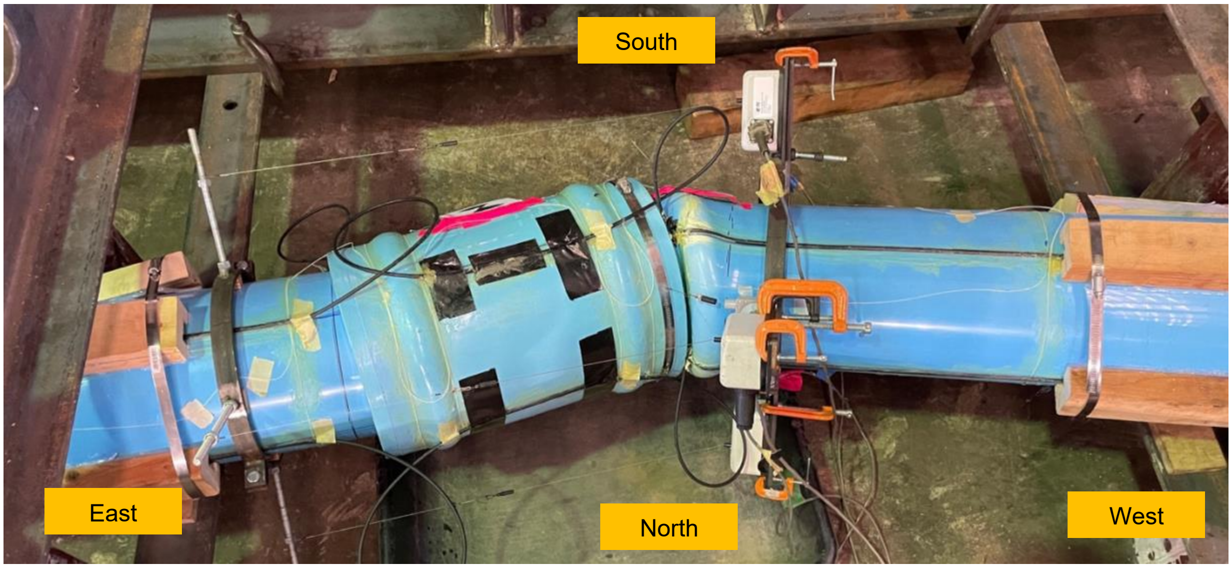

(a) Local buckling

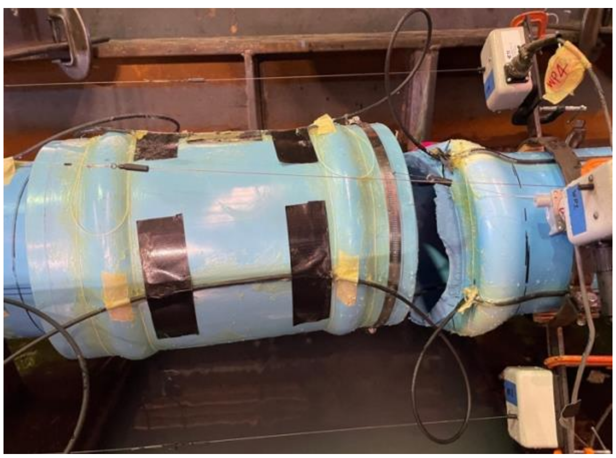

(b) Pipe failure (North side)

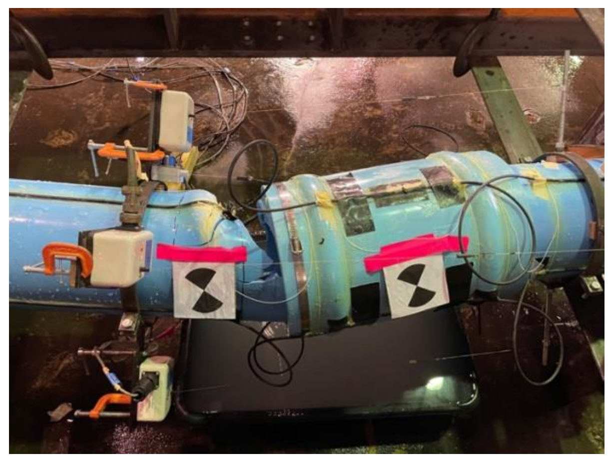

(c) Pipe failure (South side)

Figure 4-2 Failure of the specimen

4.3 Axial Strains

The axial strain data from the DFOS sensors are shown in Figure 4-3, which shows the relationship between the axial strain and axial loads at the midpoints of F1 and F2 (east pipe), and the midpoints of F7 and F8 (west pipe), measured by the longitudinal sensors. The results from both specimens show that all the pipes were experiencing compressive stresses. However, moment and local buckling were found as the compressive force developing.

For the east pipe, a moment bending towards the bottom side was detected from the beginning of the test, likely due to its self-weight. As the compressive force was applied, a moment bending towards the south side was observed. When the compressive force reached approximately 20,000 lbs, the strain measurements became erratic. This phenomenon is due to the rubber gaskets shifting and readjusting to a new equilibrium point, affecting the force transition. At around 62,000 lbs of compressive force, local buckling was observed at the edge between the fitting and the west pipe, causing a noticeable jump in the strain data. This buckling moved the specimen towards the south and bottom side, creating a bending force on the west pipe. Consequently, larger compressive strains were observed on the south and bottom sides, while less compressive strains were found on the top and north sides.

For the west pipe, no obvious bending was found at the beginning of the test. However, after the rubber gasket readjustment (i.e., when the load reached about 20,000 lbs), a bending force was observed, with the pipe bending towards the top and north sides. As the force reached 62,000 lbs, local buckling occurred, leading to larger compressive stress on the bottom side and smaller compressive stress on the top side. Due to the buckling phenomenon, significant compressive deformation was found on the north and bottom sides, where the pipe eventually failed when it was unloaded.

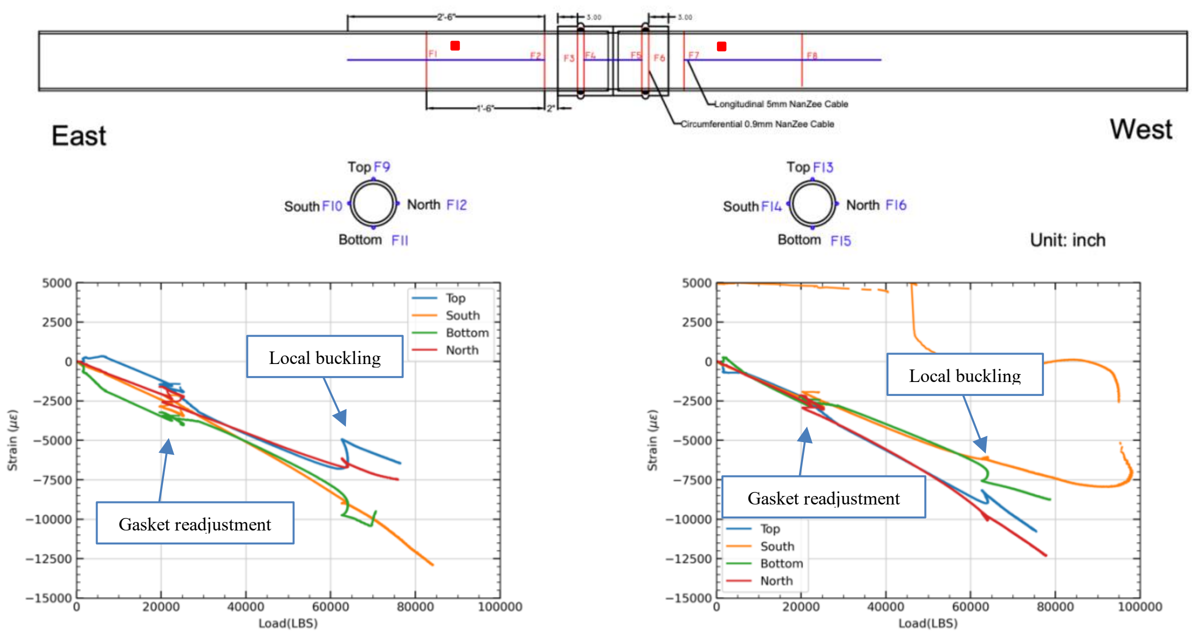

Figure 4-3 Axial strain vs load. (Left) East pipe. (Right) West Pipe.

Figure 4-4 shows the axial strain distribution of the specimen under a 70,000 lbs loading condition, after local buckling occurred. Although the specimen did not fail until the axial load reached 98,800 lbs, some strain data were not obtained after the specimen reached approximately 70,000 lbs due to the strain exceeding the maximum measuring capacity. The figures are plotted from the east to the west, with two gaps representing the boundaries between the fitting and the pipes where no DFOS was attached. When a force was applied in the axial direction, compressive strains are seen at all locations. The strain profiles on the west and east pipes are similar. The strain magnitudes at the fitting location is smaller than those measured on the pipes. This difference is because the fitting has a thicker wall, making it stiffer than the pipes. As a result, smaller strains develop on the fitting compared to the pipes.

Looking more closely at the strains developed on the pipes, it is evident that the magnitude of the strain on the two pipes differs. This disparity is again due to the local buckling that occurred on the west pipe. The local buckling induced bending moments as the axial force increased, resulting in the strain profile shown in Figure 4-4.

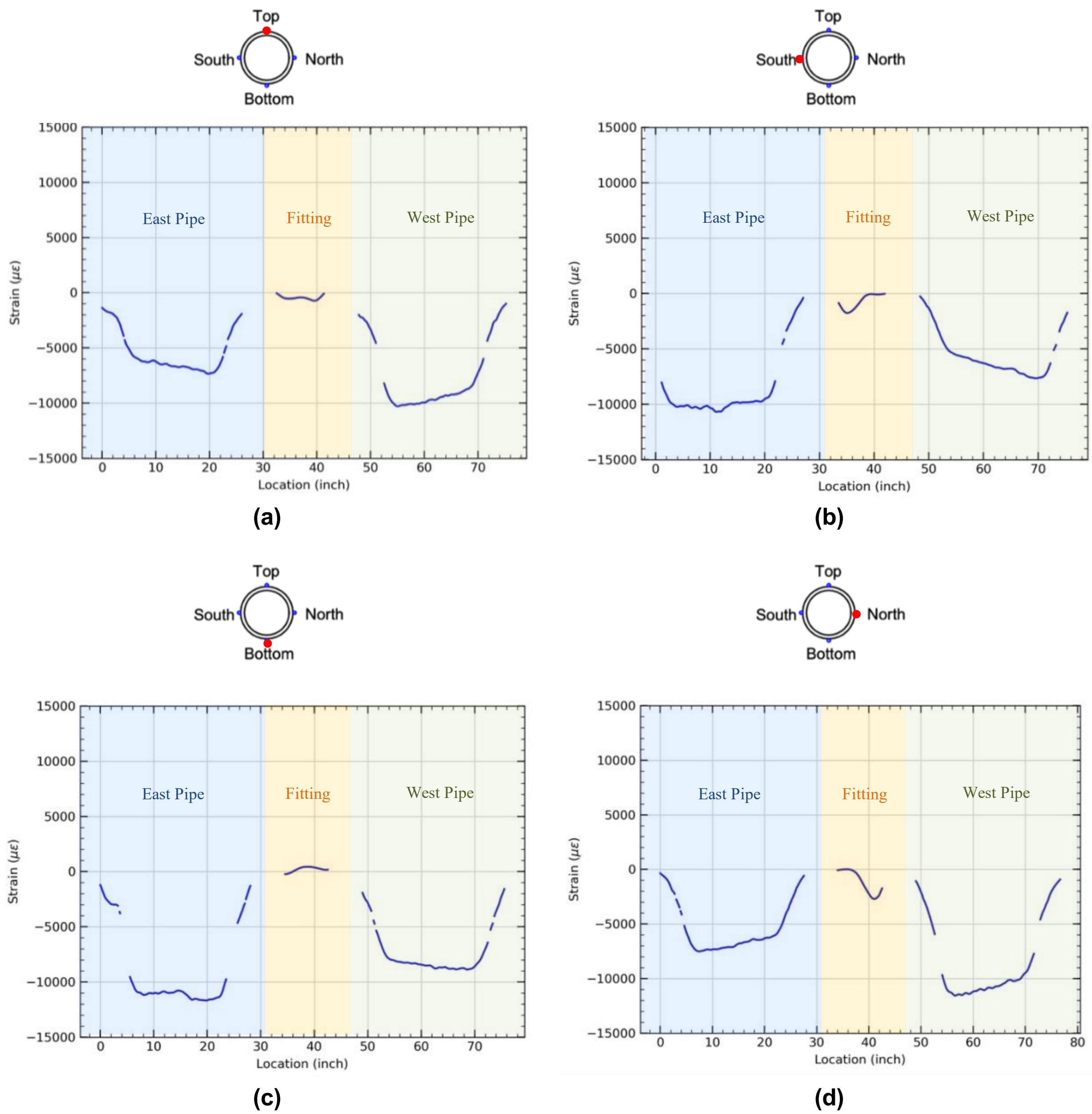

Figure 4-4 Axial strain development of the specimen under 70,000-LBS axial loading condition. (a) Top, (b) South, (c) Bottom, (d) North

4.4 Hoop Strains

The hoop strain data measured from the specimen are plotted in Figure 4-5. The figure illustrates the results obtained by the sensors positioned on the fitting (F3-F6) and the sensors on the east (F1-F2) and west pipe (F7-F8).

The results obtained from F1 and F8 (i.e., the circumferential sensors located furthest from the fitting) on the pipes show tensile strains, indicating that the pipes are expanding radially while being compressed in the longitudinal direction. This phenomenon occurs due to Poisson's effect, where strains in the circumferential direction oppose those in the longitudinal direction with a smaller magnitude. Notably, the pipe was expanding eccentrically.

Moving toward the fitting, sensors F2 and F7 also show the pattern of general expansion in the pipes; however, comparing the magnitude between the south and north as well as the magnitude between the top and bottom, it can be observed that the east pipe was expanding more on the south and the bottom, while the west pipe was expanding more on the north and the top. This is again due to the local buckling.

Comparing the strains measured on the outer side of the fitting (i.e., F3 and F6), it can be observed that the east side of the fitting was expanding much more on the south side, while the west side of the fitting was expanding on the north side. This is because, after the pipe buckled, a large rotation was found on the fitting, leading to the east pipe bearing against the south side of the fitting and the west pipe bearing against the north side of the fitting. Therefore, as the axial force pushed inward into the fitting, the pipe inevitably expanded the fitting. This mechanism is illustrated in Figure 4-6.

Looking at the sensors placed on the inner side of the fitting (i.e., F4 and F5), it can be observed that the middle section of the fitting is squatting similarly, with the south and north sides of the fitting expanding. This is again due to the local buckling, which led to a rotation on the fitting. This phenomenon caused the pipe to push and expand the fitting on the sides.

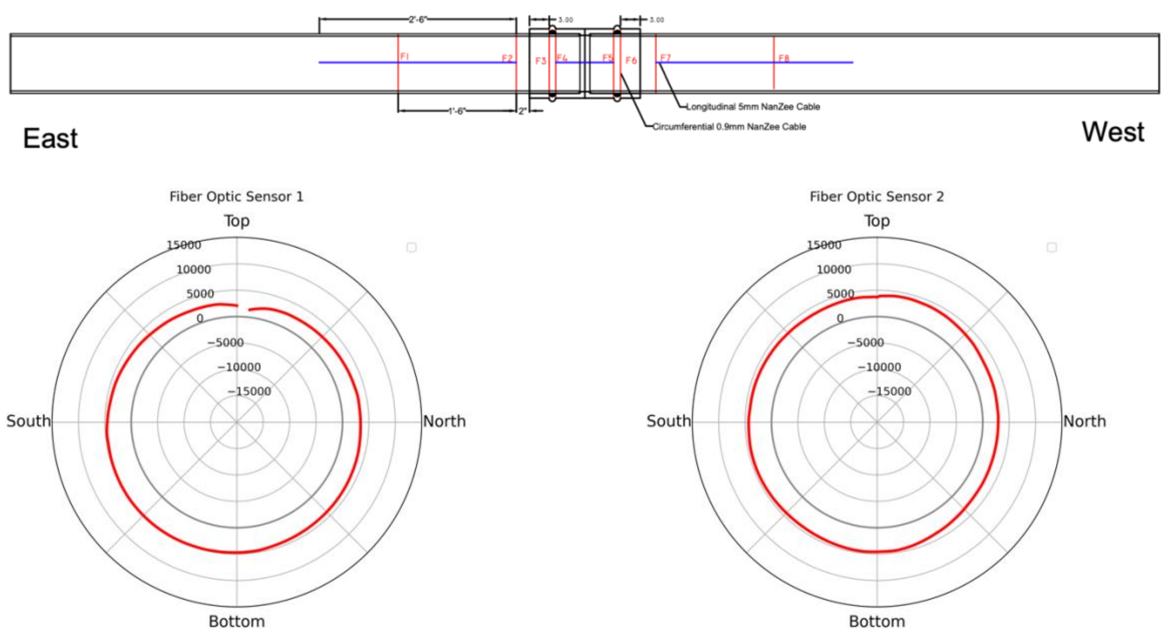

(a) Sensor F1 **(b) Sensor F2**

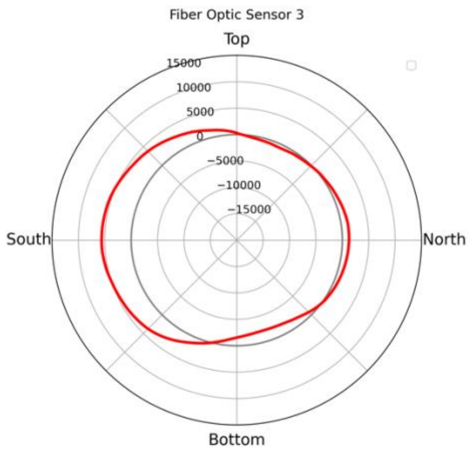

(c) Sensor F3

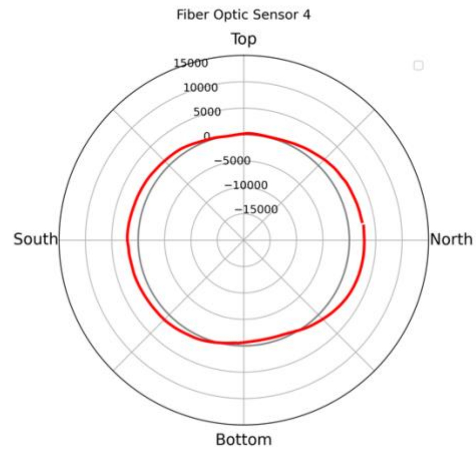

(d) Sensor F4

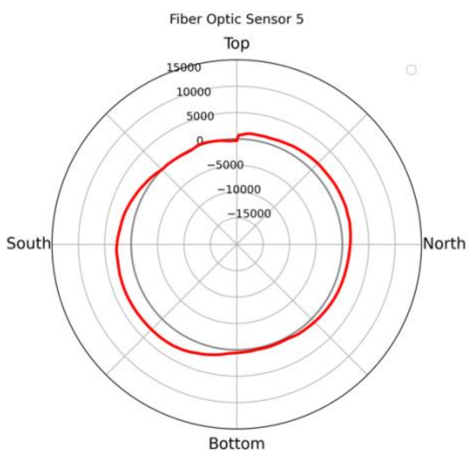

(e) Sensor F5

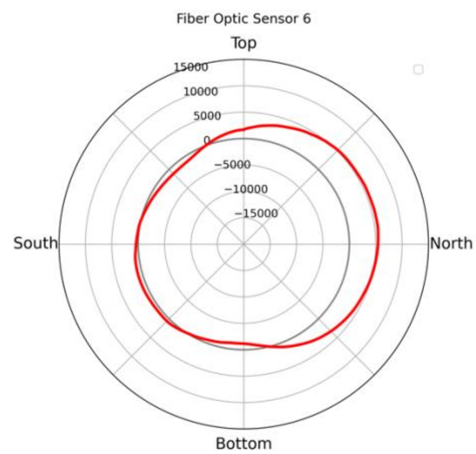

(f) Sensor F6

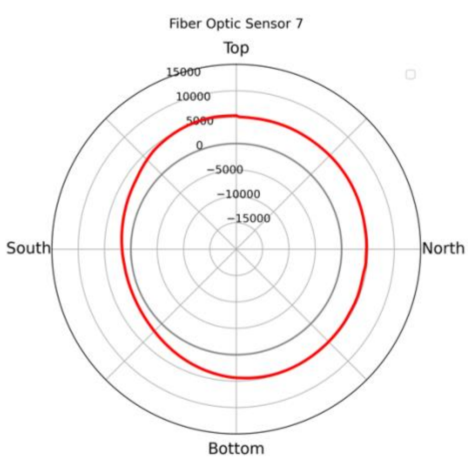

(g) Sensor F7

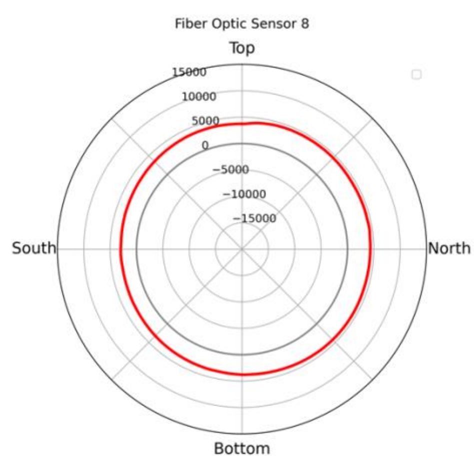

(h) Sensor F8

Figure 4-5 Strain distribution in the circumferential direction of Specimen 1 under 32,000-LBS loading condition.

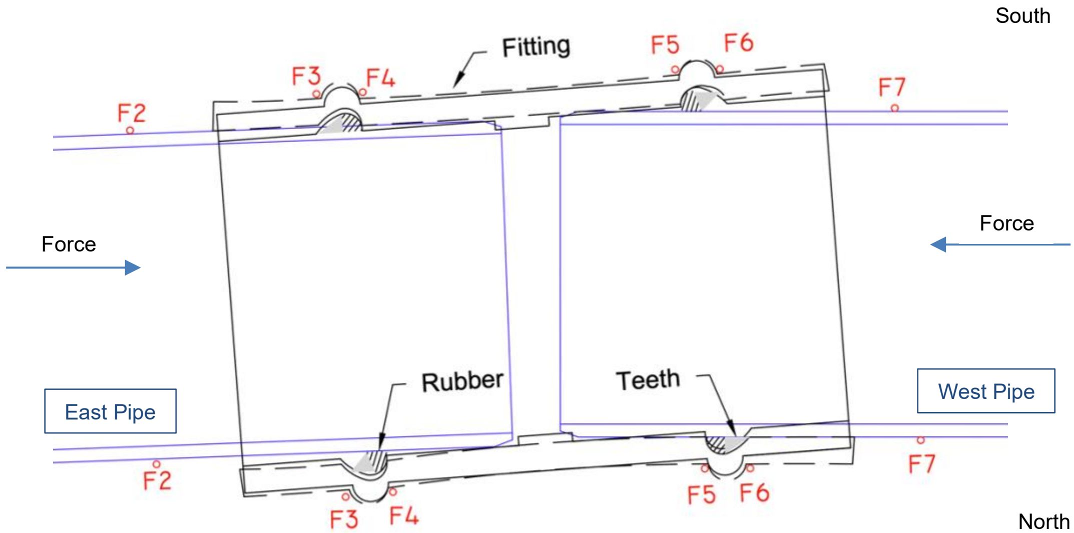

Figure 4-6 Sketch of fitting deformed mechanism.

5 Finite Element Analysis

This section presents the finite element analysis of the laboratory compression test conducted. The aim of the analysis was to investigate pipeline behaviosr by incorporating the complex material nonlinearities and contact interaction of the system components.

5.1 Overview of the Numerical Model

The geometry of the pipe and joint model follows the design of the experimental setup, as shown in Figure 4-6. The tested component consists of four main parts: two iPVC pipe segments of outer diameter D = 9 inches (229.9 mm) and thickness t = 0.65 inches (16.5 mm), sleeve joint, and rubber gasket. The interactions among the pipes, the sleeve joint and the rubber gaskets are assumed to be frictional contact, which allows for finite sliding and separation between the respective interfaces.

To reduce the computational costs, a 2D axisymmetric analysis is carried out using the finite element software ABAQUS/Standard. As shown in Figure 5-1, the mesh size of the system components is defined to assure accuracy and efficiency of the numerical solution.

The numerical analysis was performed in three consecutive steps, representing the experimental procedure: (1) contact between the pipes inserted in the sleeve joint at a distance of 1.5 inch, and the rubber gasket was established using automatic interference fit; (2) a pressure of 65 psi was applied at the internal surface of the joint pipe system; (3) The free end of the west pipe segment was subjected to compression while the free end of east pipe was restrained in the axial direction, until failure.

Sensitivity study was performed and the results demonstrated the minor effect of the RieberLok gasket to the overall pipeline resistance under compression. As a result, for simplicity, the gasket steel teeths are not modeled herein.

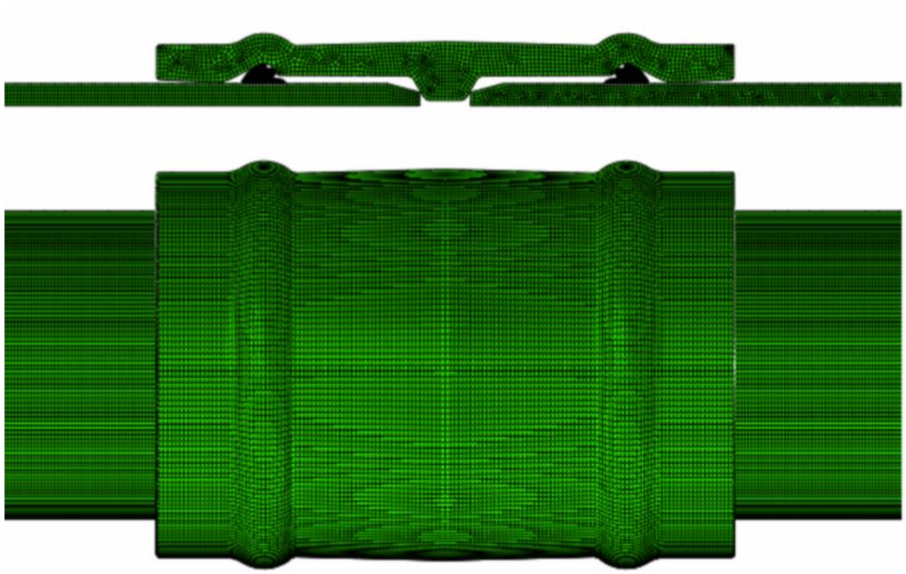

Figure 5-1 2D axisymmetric FE model mesh for axial compression test.

5.2 Determination of the Pipe parameters

The iPVC pipe material characteristics were derived from the tensile coupon test result reported in Price et al. (2018). The pipe material model is defined within the von Mises plasticity theory with isotropic hardening. The engineering stress-strain curve follows a piecewise linear curve measured in the tension coupon test (Figure 5-2). The Young's modulus is 450 ksi (3.1 GPa), the Poisson's ratio is 0.38, yield strength is 7.6 ksi (52.3 MPa) and peak tensile stress is 7.8 ksi (53.3 MPa) at 5% strain. The rubber in the seal is assumed to follow a hyperelastic Neo-Hooke model with basic constant C10 = 0.6 MPa and D1=0.002 / MPa, corresponding to a typical hardness value of 60 ShA.

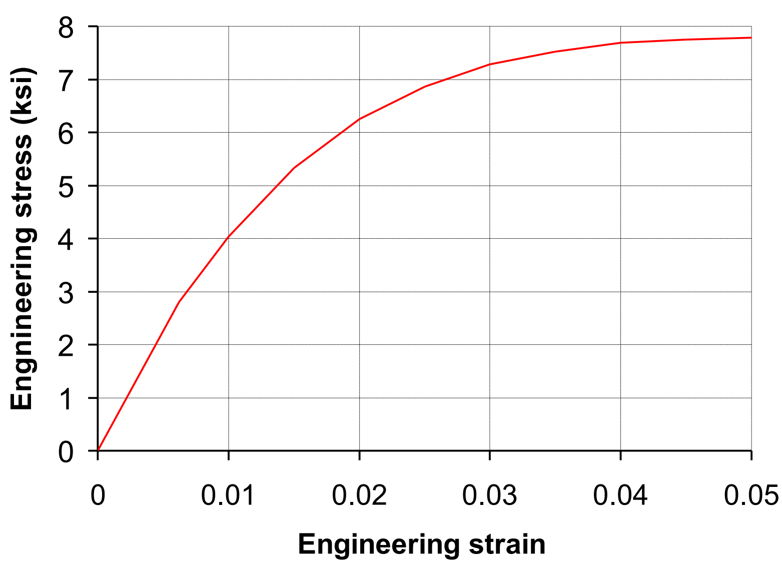

Figure 5-2 Engineering stress-strain curve for the iPVC pipe material.

5.3 Finite Element Analysis Results

This section describes the numerical results of the iPVC pipeline joint simulation under compression. It first shows the results from the model with the rubber gasket, examining initially the pipeline response under the effect of internal pressure followed by the pipeline response subjected to compression. The obtained pipeline deformation response is compared with the measured distributed strain data using DFOS, giving a better understanding of the pipeline performance.

5.3.1 Pipe response under the effect of internal pressure

This section compares the measured strain distribution along the pipeline with the results from analytical and numerical analysis, including axisymmetric and 3D continuum models, at the end of the pressurization step.

As the internal pressure is applied in the pipeline, it tends to expand in the hoop and longitudinal direction, causing the joint to displace about 4 mm before engagement of the gasket restraining mechanism. The resulting generalized plain strain state in the pipe wall is characterized by the strains in the hoop (ε_θ) and longitudinal (ε_l) direction, given by the Hooke's law:

$$\begin{aligned} \varepsilon_\theta &= \frac{1}{E}\left(\sigma_\theta - \nu\sigma_r\right) \\ \varepsilon_l &= P_i \frac{\alpha/E}{b^2/a^2 - 1}, \end{aligned} \tag{5-1}$$

Where E and n are the Young's modulus and Poisson's ratio of the pipe material, respectively; α depends on the pipe end conditions, being equal to -2n, 0, and 1-2n, for free, plane strain and closed-end conditions, respectively; $b = D/2$, and $a = \frac{D}{2} - t$ represent the outer and inner radius of the pipe cross section, respectively; and ε_θ and ε_l are the hoop and longitudinal pipe stresses, respectively.

Figure 5-3 shows the strain distribution in the pipeline circumferential direction according to the test measurements, the analytical and numerical results. The hoop strain predicted by the 2D axisymmetric and 3D analysis is in good agreement with the analytical estimation according to Eq (1), ε_θ = 800 $\mu\varepsilon$. The measured hoop stain profiles are generally greater than the theoretical prediction, and depend on the location along the specimen, being greater at the bottom compared to the top of the pipe. In particular, the hoop strain profiles closer to the specimen's midsection, measured by sensor 2 and sensor 7, indicate a slight ovalization induced by the presence of the fitting.

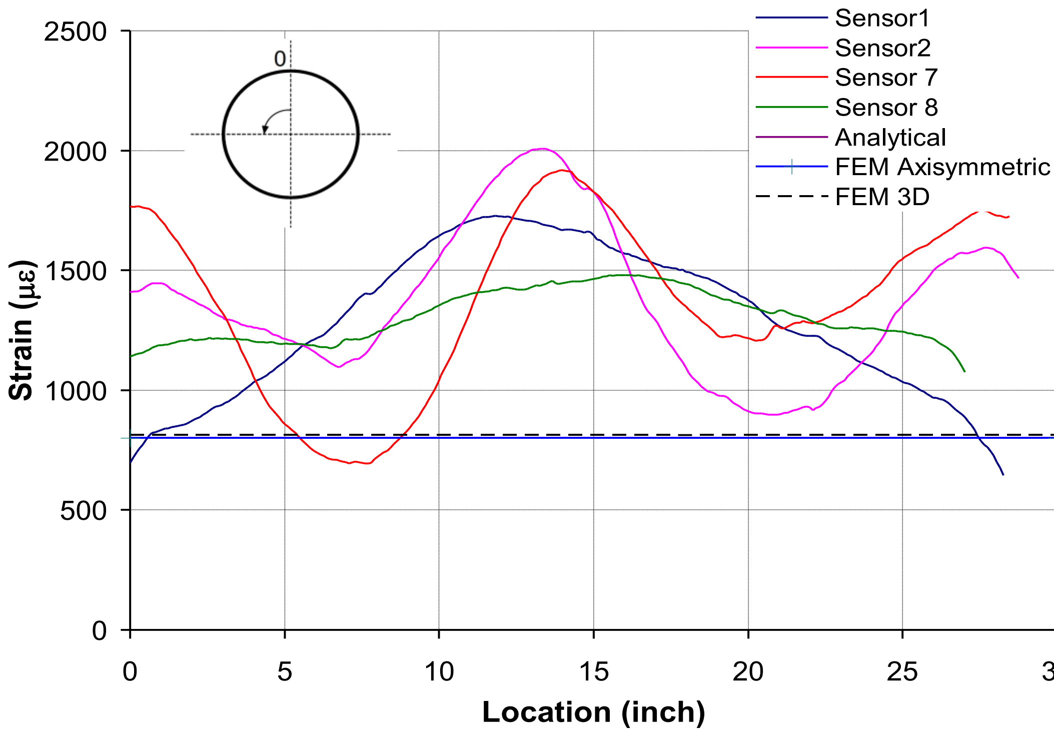

Figure 5-3 Strain distribution in the pipeline circumferential direction according to the test measurements, the analytical and numerical results.

Figure 5-4 shows the strain distribution in the pipeline longitudinal direction according to the test measurements, the analytical and numerical results. The longitudinal sensor measurements at the specimen's springline indicate positive axial strain levels that are consistent with the analytical prediction for closed-end conditions, $\varepsilon_l = 95\ \mu\varepsilon$. Conversely, the longitudinal strains at the top (Sensor 13) and bottom (Sensor 15) of the pipe segment at the west (loading) side exhibit greater compressive and tensile strains, indicating a slight bending downwards. This may be caused by the effect of the test instrumentation and the load actuator directly connected to it.

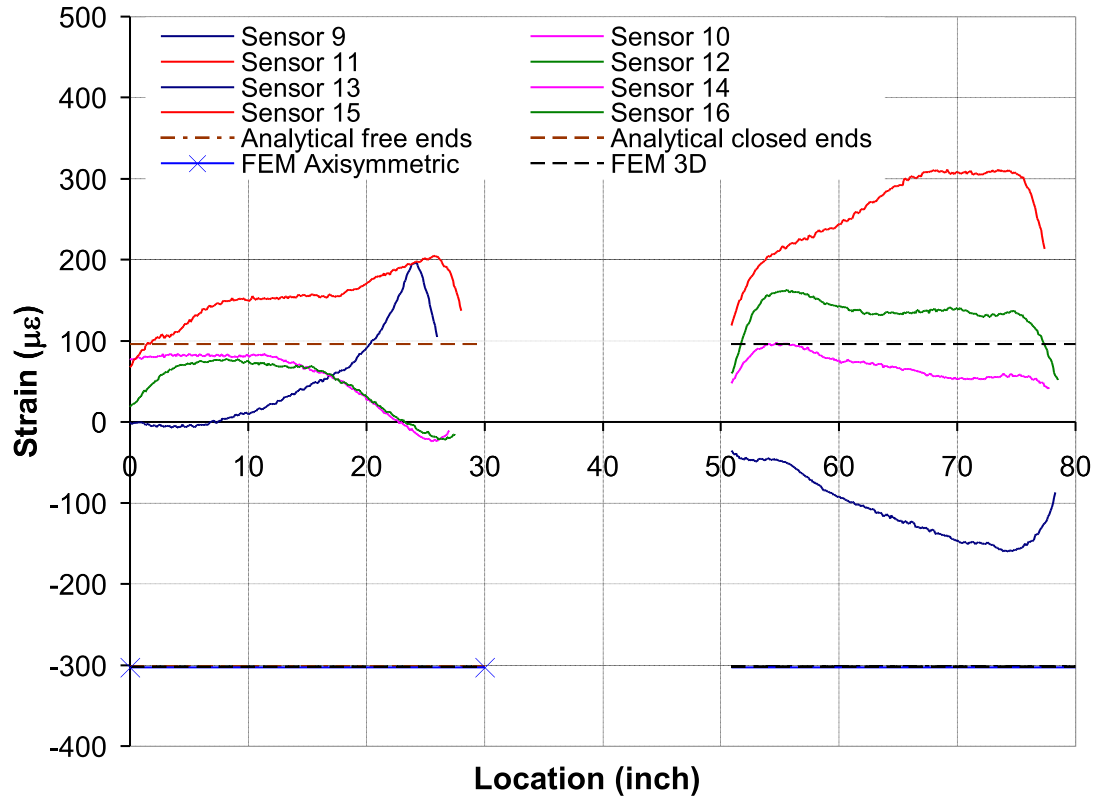

Figure 5-4 Strain distribution in the pipeline longitudinal direction according to the test measurements, the analytical and numerical results.

5.3.2 Pipe response under compressive loading

Figure 5-5 shows the iPVC pipeline joint response including the rubber gasket under compression, in five consecutive steps, until severe material damage occurs in the system, according to the numerical simulation. First, following actuator displacement at the right pipe end, the beveled section of the pipes make contact with the coupling central protrusion, further pressing against it, as the actuator load increases. (Figure 5-5 (a)). Second, the beveled section of the right-hand side pipe segment begins to bend and slide inside the coupling, sliding through the rubber gasket (Figure 5-5 (b)). Then, the beveled section of the left-hand side pipe segment bends and slides inside the coupling, sliding through the corresponding rubber gasket.

Both pipe segments and corresponding gaskets continue to slide inside the coupling, causing pipe material damage at the contact region with the coupling protrusion and at the beveled sections sliding through it. After the two beveled sections make contact with each other (Figure 5-5 (c)), the right-hand side pipe segment telescopes and bends further inside the right-hand side pipe segment (Figure 5-5 (d)). Finally, the right-hand side pipe segment bends and buckles further, moving upward and making contact with the coupling wall (Figure 5-5 (e)). This causes further rotation of the coupling, leading to global instability.

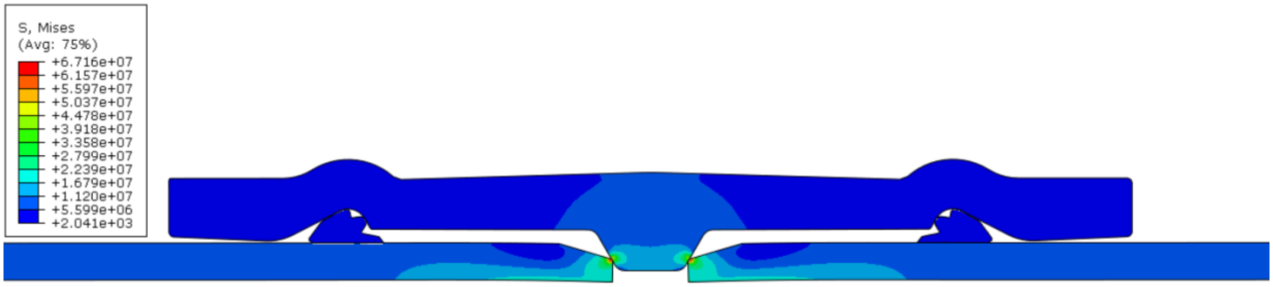
S, Mises
(Avg: 75%)
+6.716e+07
+6.157e+07
+5.597e+07
+5.037e+07
+4.478e+07
+3.918e+07
+3.358e+07
+2.799e+07
+2.239e+07
+1.679e+07
+1.120e+07
+5.599e+06
+2.041e+03

(a)

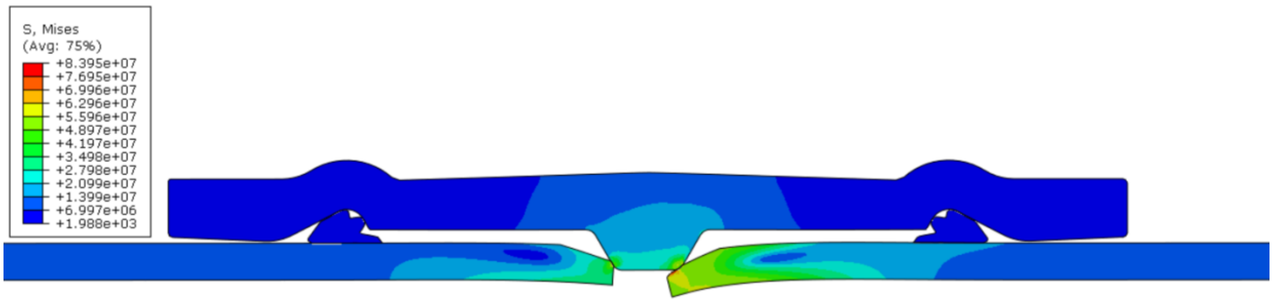
S, Mises
(Avg: 75%)
+8.395e+07
+7.695e+07
+6.996e+07
+6.296e+07
+5.596e+07
+4.897e+07
+4.197e+07
+3.498e+07
+2.798e+07
+2.099e+07
+1.399e+07
+6.997e+06
+1.988e+03

(b)

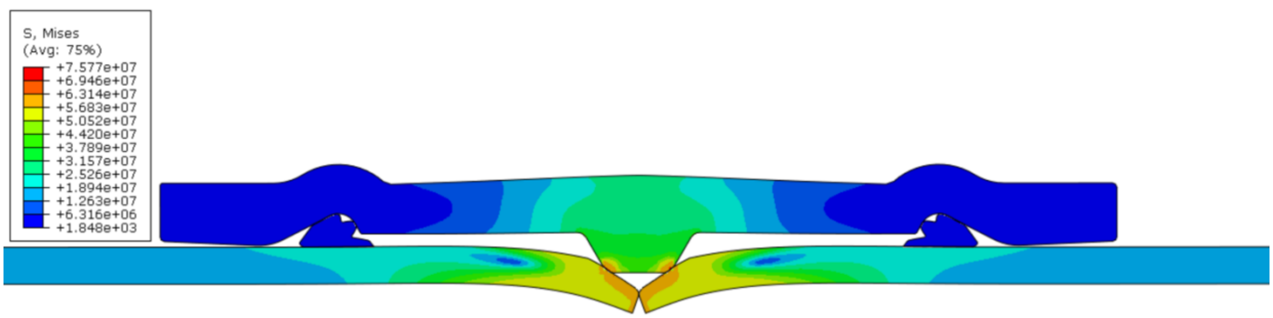
S, Mises
(Avg: 75%)
+7.577e+07
+6.946e+07
+6.314e+07
+5.683e+07
+5.052e+07
+4.420e+07
+3.789e+07
+3.157e+07
+2.526e+07
+1.894e+07
+1.263e+07
+6.316e+06
+1.848e+03

(c)

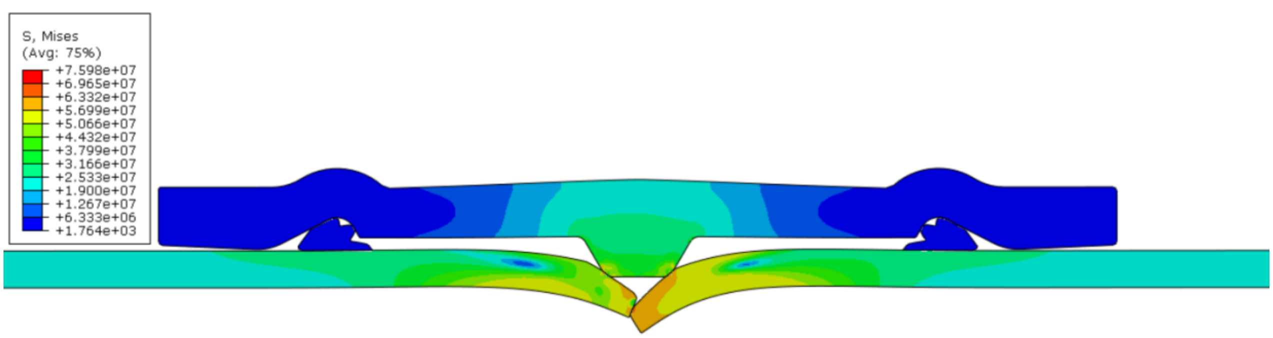
S, Mises
(Avg: 75%)
+7.598e+07
+6.965e+07
+6.332e+07
+5.699e+07
+5.066e+07
+4.432e+07
+3.799e+07
+3.166e+07
+2.533e+07
+1.900e+07
+1.267e+07
+6.333e+06
+1.764e+03

(d)

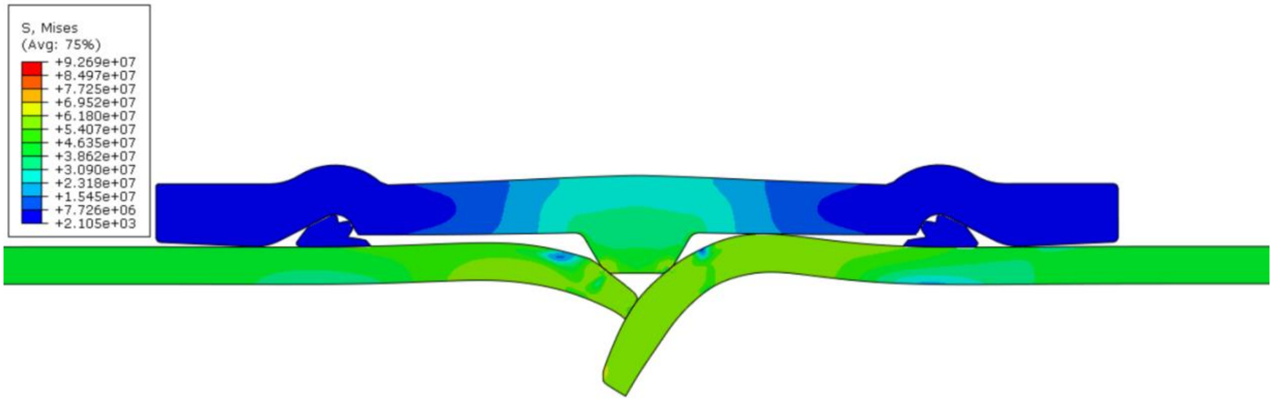

(e)

Figure 5-5 iPVC pipeline joint response under compression in five consecutive steps: (a) both pipe beveled sides come to contact with the coupling protrusion; (b) right-hand pipe bends and slides inside the coupling; (c) pipe beveled sides come to contact with each other; (d) right-hand pipe bends further and telescopes inside the left-hand side pipe segment; (e) right-hand side pipe segment buckles further, making contact with the coupling's wall.

Figure 5-6 indicates the inward deflection of the beveled sides of the left and right-hand pipe, as a function of pipe end displacement, highlighting the consecutive steps of pipeline response illustrated previously in Figure 5-5. Specifically, the two large jumps in the deflection curve of the right-hand side pipe segment (Figure 5-6) represent its first sliding inside the coupling (b), and subsequent sliding with telescoping inside the left-hand side pipe segment (d), respectively.

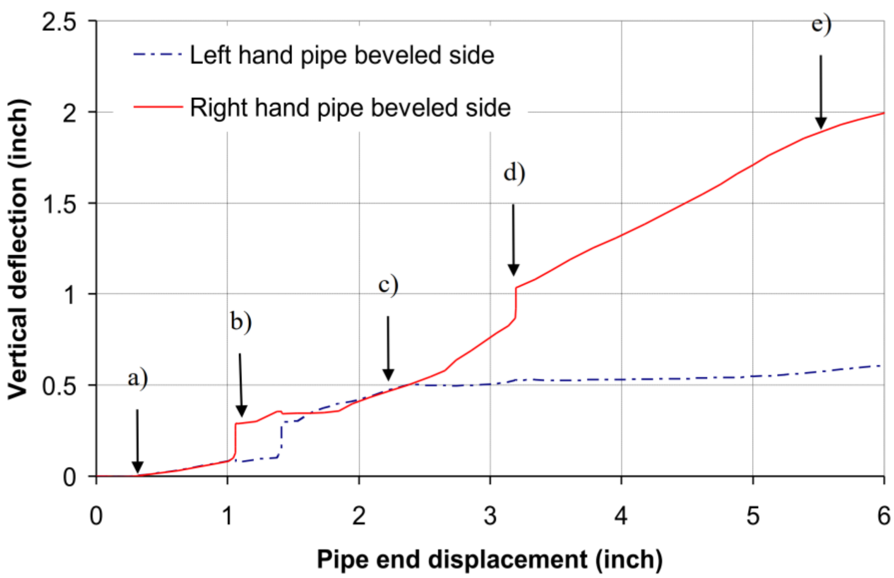

Figure 5-6 Inward deflection of the beveled sides of the left and right-hand side pipe segments as a function of the right pipe end displacement.

The numerical results show the telescoping failure mechanism associated with severe damage and local buckling of the beveled sections of the pipe segments inside the coupling, which is consistent with the experimental observations, as shown in Figure 5-7.

Figure 5-7 Severe material damage and local buckling at the beveleted sides of both iPVC pipeline segments telescoping inside the coupling, following the compression test.

5.4 Comparison of the FE model and experimental data

This section compares the numerical results of the iPVC pipeline joint simulation under compression with the experimental measurements. The axial load as a function of the joint opening, highlighting the main steps characterizing system response was first analyzed. Then, the numerical results comparing with the strain measurements using DFOS at different load levels to identify the pipeline response was performed.

5.4.1 Axial force-displacement response of the joint

Figure 5-8 presents the force-displacement curve of the pipeline joint resulting from the FE simulations and the compression test, highlighting five significant steps characterizing pipeline response.

As the beveled sides come to contact with the coupling protrusion, the load increases monotonically as a function of the joint contraction (point a), until the right-hand side pipe segment bends and slides inside the coupling (point b), causing a decrease in the load resistance. Thereafter, the right-hand side pipe segment pushes against the coupling protrusion at constant deflection rate (see Figure 5-8), increasing the load resistance until the left-hand pipe segment starts to deflect and slide inside the coupling (point c), inducing a load decrease until sliding stop and engagement of further load resistance. Subsequently, the load increases monotonically, while both pipe segments continue to slide through the corresponding gaskets inside the coupling, until they come to contact with each other (point d). Afterwards, the right-hand side pipe segment slides through the beveled section of the left-hand side pipe (point e), decreasing the load carrying capacity until the sliding rate reduces allowing for engagement of further load resistance.

The stiffness of the system according to the numerical analysis is greater than the corresponding experimental observation because of the additional constrain provided by the assumed axisymmetry. This does not include modeling of non-axisymmetric loads like gravity or initial prebending at test setup, constraining the movement along the axis of symmetry.

A 3D modeling of the pipe system is required to examine these effects, as possible future study. However, the present axisymmetric model captures the mechanical behaviour of the iPVC pipe system observed in the experimental test with the advantage of being less computationally expensive than 3D modelling.

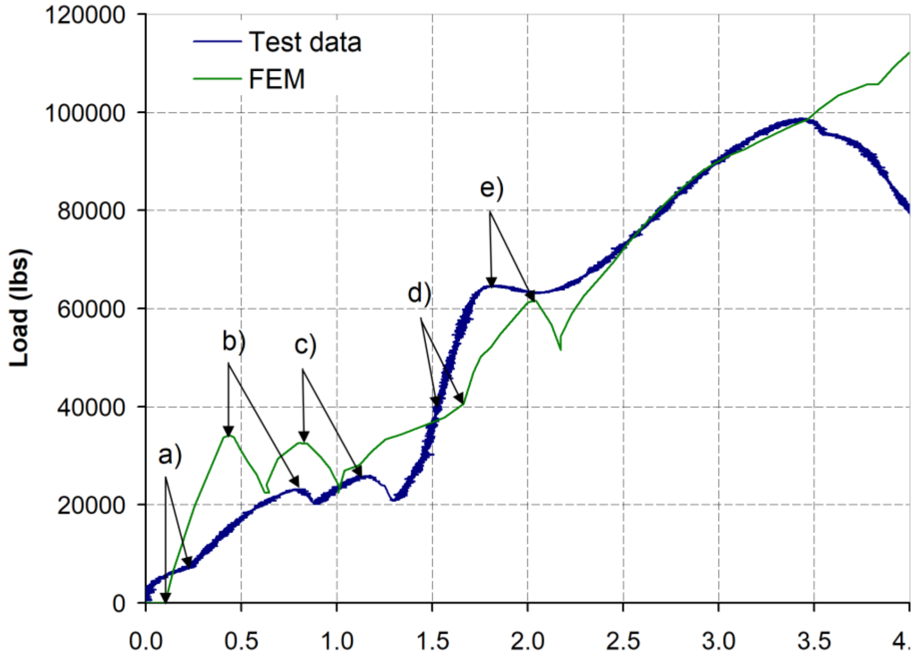

Figure 5-8 Force versus average joint closing for the iPVC pipe system: (a) both pipe beveled sides come to contact with the coupling protrusion; (b) right-hand side pipe bends and slides inside the coupling; (c) left-hand side pipe bends and slides inside the coupling (d) pipe beveled sides come to contact with each other; (e) right-hand side pipe telescopes and buckles further inside the left-hand side pipe segment.

5.4.2 Pipe strain response in the longitudinal direction

Figure 5-9 (a) and (b) show the strain distribution in the pipeline longitudinal direction according to the test measurements and numerical results, corresponding to compression load levels of 32000 lbs and 70000 lbs, respectively. The numerical results predict a uniformly distributed axial strain of 4492 $\mu\varepsilon$ and 10318 $\mu\varepsilon$, for the former and latter load level, respectively. While the DFOS measurements are consistent with the numerical results, they indicate a south-downward bending of the pipe segment at the loading (west) side even at low load levels (32000 lbs). This causes the right-hand side pipe to make contact with the edge of the coupling, inducing indentation of the pipe that starts to buckle in this region. The latter leads to further rotation of the coupling which causes the left hand pipe to bend in the opposite direction (upward north), compared to the right-hand side pipe, as shown in Figure 5-8 (b).

Figure 5-10 compares the evolution of the average axial strain as a function of the applied load in the left-hand side (east) and right-hand side (west) pipe, considering the experimental and numerical results. The left-hand side experimental and numerical results are in good agreement between each other, highlighting the critical steps of the pipe beveleded sides sliding and telescoping inside the coupling. While the average of measured axial strain is negligible at zero load, the numerical results exhibit a small initial compressive strain ε_l = -300 $\mu\varepsilon$, because of the joint opening during pressurization, as also shown in Figure 5-4. Overall, the numerical prediction slightly overestimates the measured average strain during compression, given the assumed axissymetry.

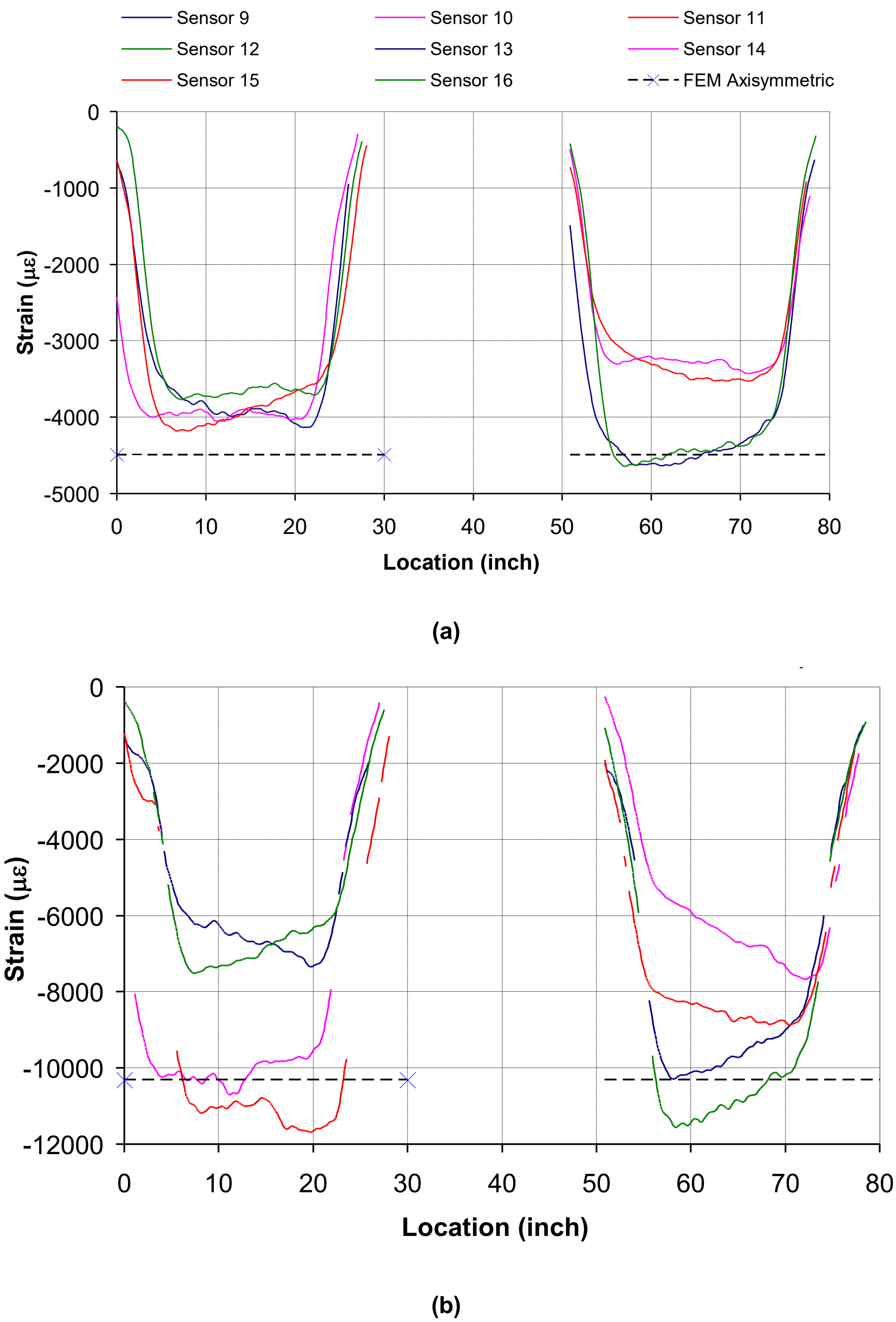

Figure 5-9 Longitudinal strain distribution in the pipeline according to the test measurements and numerical results for a compressive load of: (a) 32000 lbs; (b) 70000 lbs.

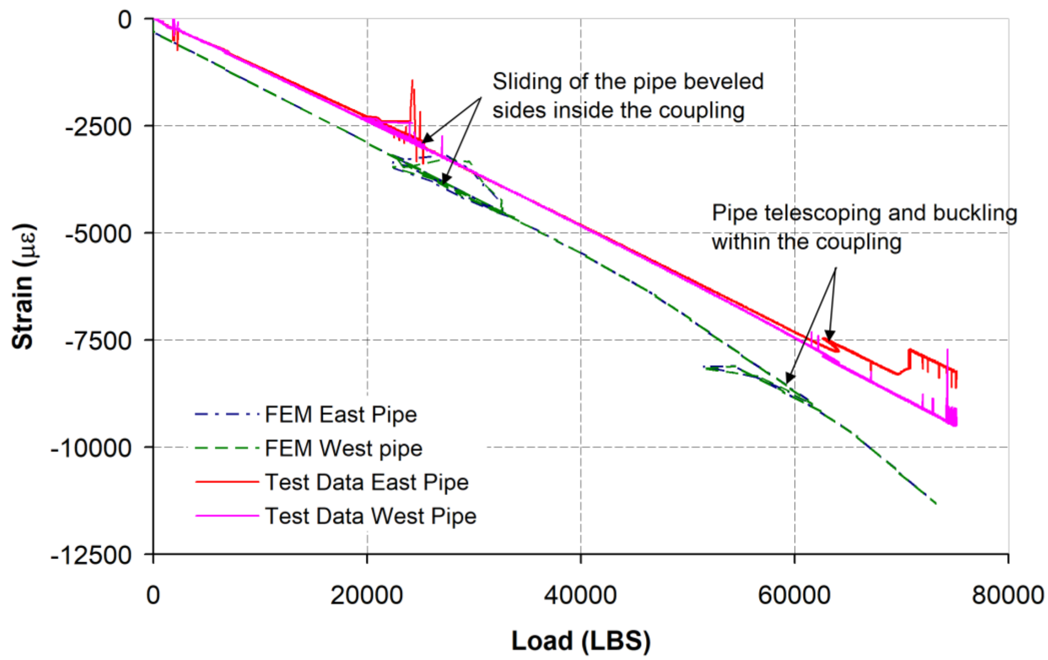

Figure 5-10 Axial strain as a function of the applied load for the east and west pipe according the experimental and numerical results.

5.4.3 Pipe strain response in the circumferential direction

Figure 5-10 (a) and (b) show the strain distribution in the pipeline circmferential direction according to the test measurements and the numerical results, corresponding to axial load levels of 32000 lbs and 70000 lbs, respectively.

The numerical results predict a uniformly distributed hoop strain of 2377 με and 4772 με, for the former and latter load level, respectively. These values tend to overestimate the corresponding average hoop strain measurements, because of the axisymmetric assumption within the numerical simulation, constraining the movement in the axial direction, as noted previously.

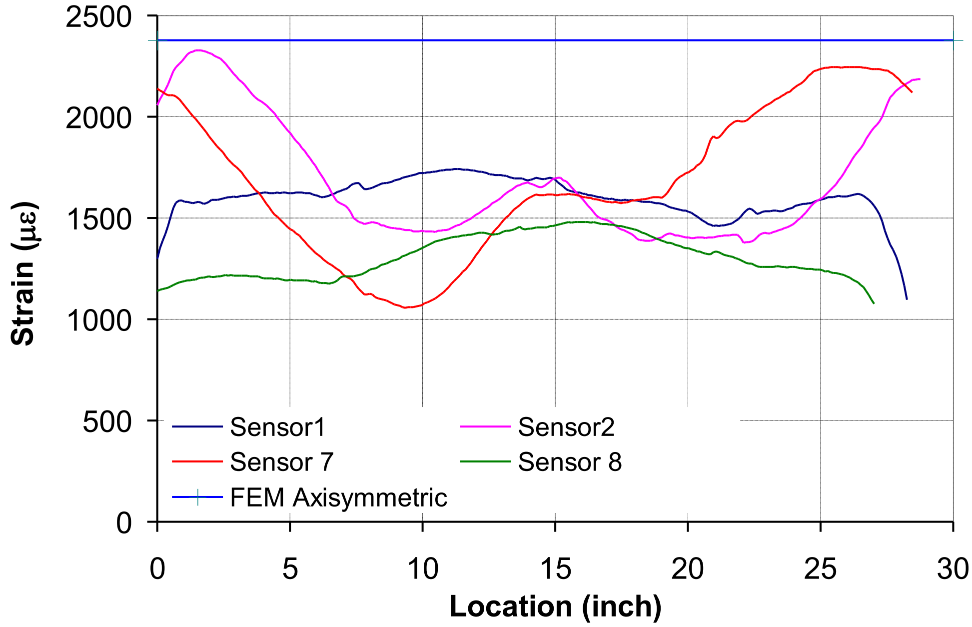

(a)

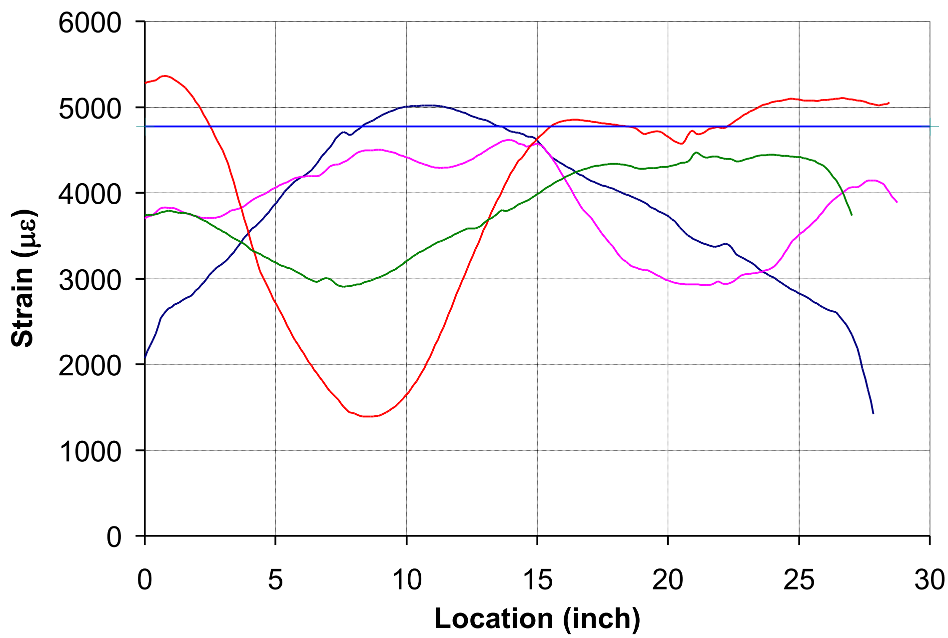

(b)

Figure 5-11 Hoop strain distribution in the pipeline according to the test measurements and numerical results for a compressive load of: (a) 32000 lbs; (b) 70000 lbs.

6 Conclusions

The report outlines the findings of compression loading experiments conducted on 8-inch AWWA C900 DR14 iPVC pipes fitted with ReiberLok rubber gaskets under compressive force. The objective was to test the pipes until severe damage or water leakage occurred.

The compression test involved pressurizing the pipes with water to approximately 65 psi and applying a monotonic inward force on the fitting along the pipeline's longitudinal axis. The specimen accomodated a peak load at about 98.8 kips of force at a displacement of about 3.46 inches across the joint. Local buckling on the west pipe was observed at this point, leading to joint rotation. The load then reduced with more joint closure. No water leakage occurred duing compression loading. The pipe failed after the specimen was unloaded and water leakage occurred. The failure was at the sleeve-west pipe interface.

The observed local buckling and associated rotational movements influenced the strain distribution and deformation/failure modes of the pipes. Axial strain measurements from distributed fiber optic sensing showed compressive strains at all locations. Although the strain profiles of the east and west pipes were similar, the magnitudes on the fitting were smaller due to its thicker wall, which provides greater stiffness. Hoop strain results indicates tensile strains on sensors F1 and F8 (furthest to the fitting), suggesting radial expansion of the pipes under compression due to Poisson's effect. Sensors F2 and F7, located on the pipes, shows that the east pipe expanded more on the south and bottom sides, while the west pipe expanded more on the north and top sides, corroborating the buckling effects. Strains on the outer side of the fitting (F3 and F6) reveals greater expansion on the south side for the east fitting and the north side for the west fitting, caused by the rotational movement due to buckling. Sensors located at the mid-section of the fitting (F4 and F5) indicates uniform squatting behavior, further evidencing the impact of buckling and subsequent rotational forces.

The numerical results provide further insight into the failure mechanisms at various loading levels. The analysis reveals that material damage begins to propagate during the early stages of joint contraction, primarily localized in the pipe region beneath the beveled sides of the pipes within the coupling. This damage progression eventually leads to local buckling and telescoping failure. The failure mechanism identified by the numerical model corresponds well with observations from experimental tests. Although the model does not capture pipeline ovalization—due to the omission of the rubber gasket's teeth—the simulation still provides a good understanding of the performance of iPVC jointed pipelines under compressive loading conditions.

7 References

PPI Pipe (n.d.). iPVC Water Pipe. https://ipvcpipe.com/eng/sub/ipvc01.php

Wu, J., Jiang, H., Su, J., Shi, B., Jiang, Y., & Gu, K. (2015). Application of distributed fiber optic sensing technique in land subsidence monitoring. Journal of Civil Structural Health Monitoring, 5(5), 587-597.

Appendix A: Distributed Fiber Optic Sensing

Using the physical properties of light, fiber-optic sensing can detect changes in temperature, strain, and other parameters when light travels along a fiber, which uses fiber-optic cables as sensors and can measure over long distances at 100 to 1000s of points on a single cable or multiplexed cables depending on the analyzer used. Compared to the other sensing technologies, fiber-optic sensing has distinct advantages such as small size, light weight, and strong resistance to corrosion and water. Distributed fiber optic sensing consists of two main components, an analyzer, and fiber-optic cables. LUNA ODiSI 6000 series integrator was used as the analyzer, and NanZee Sensing Technology Co manufactured the fiber-optic cables in the experiments.

LUNA Interrogator

Figure A-1. LUNA ODiSI 6000 Series optical distributed sensor interrogator (LUNA, 2022)

LUNA ODiSI 6104 is an optical distributed sensor interrogator that can provide thousands of strain or temperature measurements per meter of a single high-definition fiber sensor. High-Definition H.D.D) Sensors - Strain & Temperature (HD-SC) temperature sensors utilize an advanced interrogation mode of the ODiSI to increase the accuracy of measurements when the sensors are subjected to strain, such as in embedded and surface-mount installations. It can achieve a sensor gauge pitch (the distance between two measurement points) as small as 0.65 mm, a sensor length of up to 100 m, and a measurement rate of up to 250 Hz with an accuracy of less than ±1 microstrain.

Fiber-optic Cable

Two types of fiber optic cables manufactured by NanZee Sensing Technology Co. were used; (a) 5 mm diameter armored cable (NanZee 5mm) and (b) 0.9 mm diameter cable (NanZee 0.9mm). Table A-1 lists the information on the cables. The difference between the two cables is the thickness and material of the coating. NanZee, a 5mm cable, provides a sheath layer and steel reinforcement, resulting in better protection to the optical core; hence, it can be used for the actual field application. The coating of NanZee 0.9mm cable is thinner than NanZee 5mm cable. NanZee 0.9mm cable has less protection, but a more sensitive strain response is achieved.

Table A-1 Schematic illustration of the selected strain sensor cable (Wu et al., 2015)

Brand	NanZee Sensing Technology Co.	NanZee Sensing Technology Co.
Model	NZS-DSS-C07	NZS-DSS-C02
Cross section	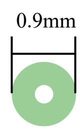	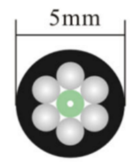
Side view